Volume 17 | Number 12 | 28 March 2015 | Pages 7583–8284

PCCP

Physical Chemistry Chemical Physics

www.rsc.org/pccp

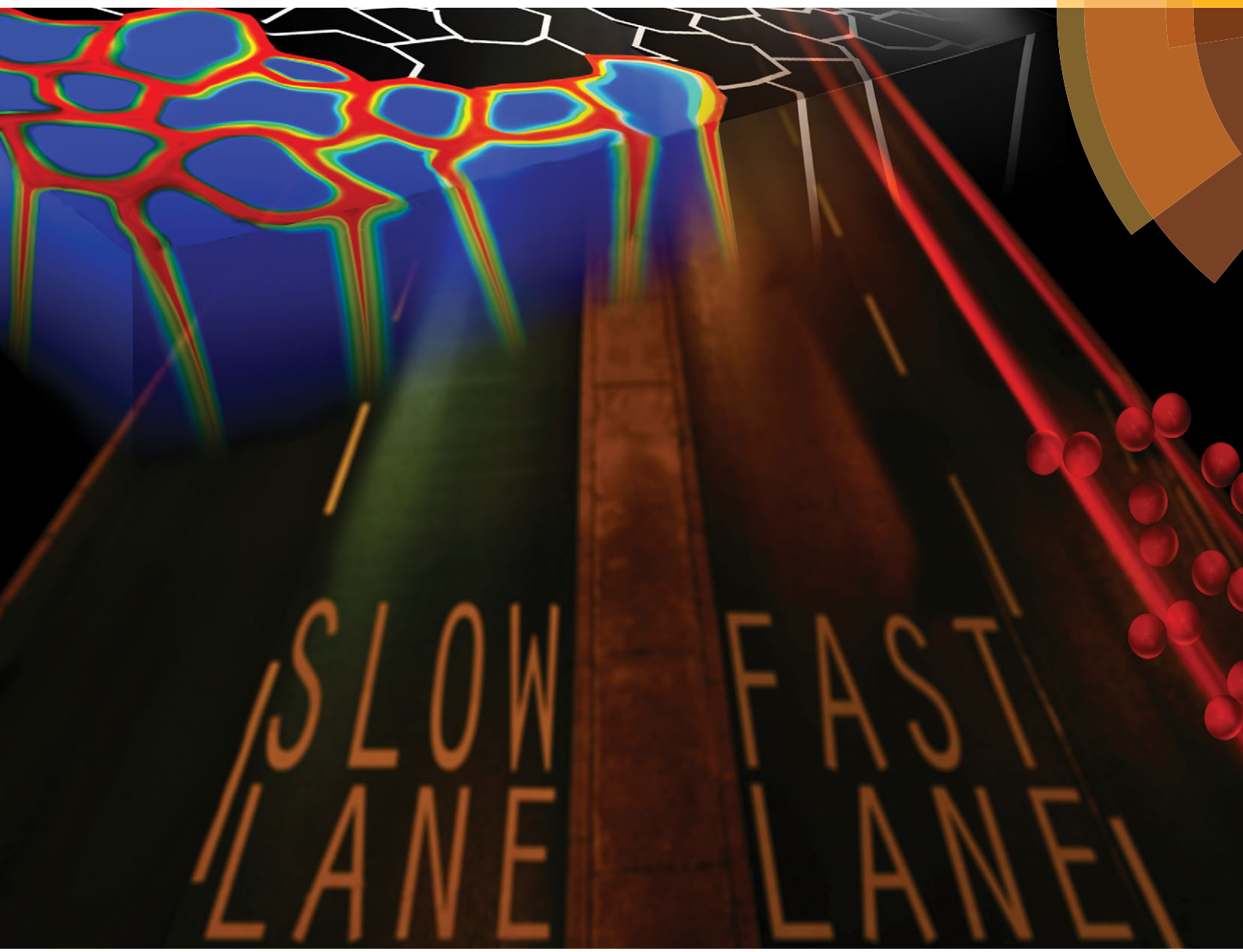

ISSN 1463-9076

ROYAL SOCIETY OF CHEMISTRY

PAPER

Jürgen Fleig *et al.*

Fast oxygen exchange and diffusion kinetics of grain boundaries in Sr-doped $LaMnO_3$ thin films

PCCP

PAPER

View Article Online
View Journal | View Issue

Cite this: *Phys. Chem. Chem. Phys.*, 2015, **17**, 7659

Fast oxygen exchange and diffusion kinetics of grain boundaries in Sr-doped $LaMnO_3$ thin films

Edvinas Navickas,†[a] Tobias M. Huber,†[a] Yan Chen,[b] Walid Hetaba,[c] Gerald Holzlechner,[a] Ghislain Rupp,[a] Michael Stöger-Pollach,[c] Gernot Friedbacher,[a] Herbert Hutter,[a] Bilge Yildiz[b] and Jürgen Fleig*[a]

Received 21st November 2014,
Accepted 5th January 2015

DOI: 10.1039/c4cp05421k

www.rsc.org/pccp

In this study, the contribution of grain boundaries to the oxygen reduction and diffusion kinetics of $La_{0.8}Sr_{0.2}MnO_3$ (LSM) thin films is investigated. Polycrystalline LSM thin films with columnar grains of different grain sizes as well as epitaxial thin films were prepared by pulsed laser deposition. ^{18}O tracer exchange experiments were performed at temperatures from 570 °C to 810 °C and subsequently analyzed by secondary ion mass spectrometry (SIMS). The isotope concentration depth profiles of polycrystalline films clearly indicate contributions from diffusion and surface exchange in grains as well as in grain boundaries. Measured depth profiles were analyzed by finite element modeling and revealed the diffusion coefficients D and oxygen exchange coefficients k of both the grain bulk and grain boundaries. Values obtained for grain boundaries (D_{gb} and k_{gb}) are almost three orders of magnitude higher than those of the grains (D_g and k_g). Hence, grain boundaries may not only facilitate fast oxygen diffusion but also fast oxygen exchange kinetics. Variation of the A-site stoichiometry ($(La_{0.8}Sr_{0.2})_{0.95}MnO_3$) did not lead to large changes of the kinetic parameters. Properties found for epitaxial layers without grain boundaries (D_b and k_b) are close to those of the grains in polycrystalline layers.

1. Introduction

Sr-doped $LaMnO_3$ (LSM) is known for its use in cathodes of solid oxide fuel cells (SOFC) for high temperature applications,[1] particularly in conjunction with doped zirconia (composite electrode).[2–5] LSM exhibits relatively good chemical stability, temperature expansion compatibility with the electrolyte and acceptably high electronic conductivity. At high temperatures LSM tends to react with the electrolyte and may form secondary phases at the cathode/electrolyte interface,[6,7] which can be retarded by an A-site deficiency.[7] However, the ionic conductivity at SOFC operation temperatures is quite low.[8] This is crucial for the oxygen reduction reaction (ORR) at the SOFC cathode, since this reaction may take place close to the three phase boundary (TPB) but can also run *via* a bulk path[7,9] provided mixed ionic and electronic conducting electrodes are used. Owing to its low ionic conductivity, the bulk path in LSM is often regarded to be relevant particularly for thin films[8–17] or for porous electrodes upon cathodic polarization.[18–20]

Moreover, there is an open question regarding the bulk path in LSM: how much do grain boundaries contribute to the overall oxygen reduction rate? Some studies dealt with the effect of crystallographic orientation[21] or substrate[22] on ionic conductivity in LSM thin films. Different electronic properties of grain boundaries compared with grain surfaces were found by scanning tunneling microscopy (STM) studies on LSM layers.[23,24] This also suggests a different catalytical activity for ORR at the grain boundaries, but quantitative data are not available yet. Impedance spectroscopic measurements on thin film microelectrodes can reveal information on the relative importance of bulk path and surface path[11] and can even distinguish whether the bulk path for ORR is limited by the surface reactions or by transport through the bulk.[14] However, information on grain boundary effects can hardly be resolved unambiguously by this technique.

^{18}O exchange experiments followed by secondary ion mass spectrometry (SIMS) analysis – also called isotope exchange depth profiling (IEDP) – is a powerful technique to probe oxygen surface exchange and oxygen diffusion kinetics and/or to visualize the active ORR sites.[25–34] There are also some IEDP studies on sintered LSM[31,32,34] where it was found that grain boundary diffusion does have an influence on the overall oxygen transport in polycrystalline LSM samples. Quantitative information on the oxygen exchange properties of the grain boundaries was not deduced from those measurements. Additional information on oxygen diffusion in grains and grain boundaries of LSM, particularly in LSM thin

[a] *Institute of Chemical Technologies and Analytics, Vienna University of Technology, Getreidemarkt 9, Vienna A-1060, Austria. E-mail: J.Fleig@tuwien.ac.at*
[b] *Department of Nuclear Science and Engineering, Massachusetts Institute of Technology, 77 Massachusetts Avenue, 24-107, Cambridge, MA 02139, USA*
[c] *University Service Centre for Transmission Electron Microscopy, Vienna University of Technology, Wiedner Hauptstr. 8-10, Vienna A-1040, Austria*
† E. Navickas and T. M. Huber contributed equally to this work.

films with active ORR bulk path, are therefore vital for understanding their role, especially in nanoscaled thin-film structures.

In this study, we report results of IEDP experiments revealing the strong acceleration effect of grain boundaries for oxygen surface exchange and oxygen diffusion in LSM thin films prepared by pulsed laser deposition. The ^{18}O isotope exchange experiments were performed between 560 and 810 °C on polycrystalline LSM layers with different grain widths and on epitaxial layers. The isotope depth profiles were analyzed by numerical finite element modeling. In order to investigate the relevance of A-site non-stoichiometry, nominally stoichiometric ($La_{0.8}Sr_{0.2}MnO_3$) and A-site deficient LSM ($(La_{0.8}Sr_{0.2})_{0.95}MnO_3$) thin films were investigated. These measurements allowed for the first time the determination not only of the grain boundary diffusion coefficient but also of the grain boundary surface exchange coefficient k_{gb} of LSM thin films.

2. Experimental section

2.1 LSM thin film preparation

LSM thin films were prepared by pulsed laser deposition (PLD). The nominally stoichiometric PLD target, denoted as LSM100, was produced from $La_{0.8}Sr_{0.2}MnO_3$ (Sigma Aldrich) powder, which was isostatically pressed into pellets and sintered for 12 h at 1200 °C in air. The PLD target of nominally deficient LSM95 ($(La_{0.8}Sr_{0.2})_{0.95}MnO_3$) was prepared from powder synthesized by the Pechini method. The preparation route is described in more detail elsewhere.[17] The as-synthesized LSM95 powders were subsequently calcined at 1100 °C for 6 h in air with a ramping rate of 3 °C min^{-1} and afterwards pressed into pellets and sintered at 1300 °C in air for 20 h.

All polycrystalline LSM layers were deposited on YSZ (100) (ZrO_2 with 9.5 mol% Y_2O_3, CrysTec GmbH, Germany) single crystal substrates. The deposition was performed in oxygen atmosphere at 4×10^{-2} mbar oxygen pressure using a KrF excimer laser with a wavelength of 248 nm and a pulse frequency of 10 Hz. The laser beam energy was set to 400 mJ per pulse and a target-substrate distance of 6 cm was used. Different film growth temperatures ranging from 600 °C to ≥810 °C were employed to vary the grain width of the thin films with columnar grains. The substrate temperature was measured by an IR pyrometer (Heitronics KT-19.99, Germany).

Epitaxial LSM95 and LSM100 layers were deposited on $SrTiO_3$ (STO) (100) (CrysTec GmbH, Germany) single crystals at 650 °C under 1.3×10^{-2} mbar oxygen pressure. The films were cooled down to room temperature in 2.7 mbar oxygen pressure. The other PLD parameters were the same as for the polycrystalline LSM layer preparation.

2.2 Thin film characterization

X-ray diffraction (XRD) 2θ–ω scans and reciprocal space mapping (RSM) of epitaxial and polycrystalline layers were performed with a high resolution four-circle Bruker D8 Discover diffractometer, which is equipped with a Göbel mirror, four-bounce Ge(220) channel-cut monochromator, Eulerian cradle, and a scintillation counter, using Cu $K_{\alpha 1}$ radiation. The thickness of the epitaxial layers was analyzed by X-ray reflectivity (XRR) measurements performed on Rigaku Smartlab diffractometer equipped with 2-bounce Ge (220) channel-cut monochromator using Cu $K_{\alpha 1}$ radiation. From XRR measurements (not shown) the thickness of these epitaxial layers was found to be 28 nm for LSM100 and 29 nm for LSM95.

The thickness of the polycrystalline LSM layers was controlled by deposition time and later determined by scanning electron microscopy (SEM) (FEI Quanta 200 FEG, Netherlands) and transmission electron microscopy (TEM) (FEI TECNAI-20) from cross-section images. Values ranging from 170 nm to 212 nm were found. The grain width of LSM layers was estimated by two techniques: atomic force microscopy (AFM) (NanoScope V, Bruker Nano) and TEM. In the first case, the surface morphology of LSM95 and LSM100 thin films was characterized using AFM tapping mode. The resulting AFM micrographs were then analyzed by the linear intercept method. In TEM measurements the average column widths were determined from the available images.

2.3 Isotope exchange depth profile (IEDP) experiments

The isotope exchange was performed in a gas tight exchange chamber at 200 mbar 97.1% ^{18}O oxygen (Campro Scientific, Germany) at temperatures ranging from 570 °C to 810 °C. The isotope exchange took place for 10 to 60 minutes depending on temperature. After the exchange the sample was quickly quenched to room temperature in ambient air. The evacuation step performed at diffusion temperature before filling the exchange chamber with tracer gas would annihilate any chemical pre-equilibration. Therefore such a pre-equilibration was not performed and a contribution of chemical diffusion to the tracer profile could not be avoided. This, however, is expected to be of negligible relevance due to the small concentration of oxygen vacancies in LSM: any change of the vacancy concentration by chemical diffusion involves only a very small amount of tracer molecules. Further information dealing with similar exchange experiments on Sr-doped $LaCoO_3$ thin layers are given in ref. 33.

The resulting ^{18}O depth profiles were subsequently investigated by time-of-flight secondary ion mass spectrometry (ToF-SIMS) (ION-TOF GmbH, Germany ToF-SIMS 5). For these SIMS measurements the collimated burst alignment (CBA) mode with Bi_3^{++} primary ions (25 keV) was used, which allows accurate determination of ^{18}O fractions in a broad intensity range.[35,36] Negative secondary ions were analyzed in areas of 30×30 μm^2, using a raster of 256×256 measurement points. For the sputtering of material, 1 keV Cs^+ ions were applied with a sputter crater of 300×300 μm^2 and sputtering ion current of 70 nA. The charging of surfaces was compensated by an electron flood gun. The depth profiles of the isotope fraction ($f(^{18}O)$) were obtained by normalizing integrated intensities I of ^{18}O and ^{16}O according to

$$f(^{18}O) = \frac{I(^{18}O)}{I(^{16}O) + I(^{18}O)} \quad (1)$$

3. Results and discussion

3.1 X-Ray diffraction (XRD) measurements

The structure and phase purity of the layers was checked by XRD. In Fig. 1 the diffraction patterns of nominally stoichiometric $La_{0.8}Sr_{0.2}MnO_3$ (LSM100) and A-site deficient ($(La_{0.8}Sr_{0.2})_{0.95}MnO_3$) (LSM95) are shown over the entire 2Θ range measured. All visible peaks could be assigned to either the yttria stabilized zirconia (YSZ) substrate or the LSM thin films. Both diffraction patterns are dominated by the intense substrate peaks overshadowing the (011) and (022) peaks of LSM. Furthermore, the K_β peaks of the single crystal YSZ are visible since the Cu K_β radiation was not completely filtered. A rhombohedral distortion of the LSM lattice was not found, but cannot be excluded due to the low intensity of the thin film signals. Pseudo-cubic out-of-plane lattice parameters were calculated from these diffraction patterns, yielding 3.914 ± 0.004 Å for the LSM100 and 3.946 ± 0.003 Å for the LSM95 thin film. A preferential grain orientation (001) can be concluded from these thin film diffraction patterns.

Owing to the similar lattice parameters of LSM and STO, preparation of LSM100 and LSM95 on STO substrates leads to epitaxial layer growth.[21,37] The microstructure of the deposited layers was checked by 2θ–ω scans (Fig. 2a) and by reciprocal space mapping (Fig. 2b). The X-ray diffractograms indicate that both LSM layers are with (001) out-of-plane orientation and epitaxial. The small peaks in 2θ–ω scans around the (001) and (002) peaks (Fig. 2a) are thickness fringes, which come from constructive interference of X-rays reflected from the film and the substrate interface. The presence of such thickness fringes is an indication of the high quality of the film, with a smooth surface and film-substrate interface. As one can see from reciprocal space maps (RSM) (Fig. 2b), the peaks of LSM100 and LSM95 are located right beneath those of the STO substrate, which indicates that the in-plane lattice parameter of the LSM films epitaxially match to that of the STO substrate (3.905 Å). Keeping in mind that the LSM bulk lattice parameter (3.88 Å) (ref. 38) is smaller than for STO, this should lead to a tensile strain, which was also observed in another study.[38]

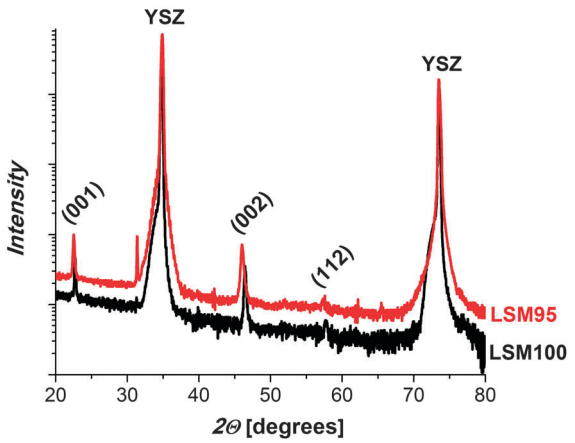

Fig. 1 θ–2θ scans of polycrystalline LSM95 and LSM100 thin films deposited at 695 °C on YSZ substrates.

3.2 The microstructure of LSM films

The surface morphology of epitaxial and polycrystalline LSM layers deposited at 600, 700 and ≥810 °C was checked by atomic force microscopy (AFM) (Fig. 3). Layers prepared on STO substrates have a smooth surface with RMS roughness lower than 1 nm. Layers deposited on a YSZ substrate show a grain microstructure at the surface with a higher RMS roughness. The films deposited at lower temperatures show finer microstructures. Supported also by TEM (see Fig. 3), these visible structures are identified as the columnar grains, and the coarsening with increasing substrate temperature therefore reflects an increasing grain width also due to the higher adatom mobility at the surface during deposition. The grain width was estimated from several line scans of AFM micrographs. This lead to mean grain width values of *ca.* 30 nm for LSM100 deposited at 600 °C, *ca.* 40 nm for LSM100 deposited at 700 °C, *ca.* 60 nm for LSM95 deposited at 600 °C and *ca.* 70 nm for LSM95 deposited at 700 °C. Accordingly, the mean grain size of LSM95 is about 30 nm larger than that of stoichiometric LSM. This is most probably caused by the different cation defect concentration which also modifies film growth and grain growth kinetics.

Layers formed at ≥810 °C have less pronounced microstructural features and in this case a grain width was estimated from TEM cross-section bright-field images. The TEM measurements were performed on LSM100 layers and examples are shown in Fig. 3. The measurements confirmed the columnar grain growth but also revealed some variation in grain width within a single layer. Keeping the limited statistics in mind, results found from TEM for LSM100 deposited at 600 °C and 700 °C are in a good agreement with AFM results, *i.e.* again *ca.* 30 and *ca.* 40 nm, respectively. The LSM100 layer deposited at ≥810 °C showed slightly larger grains in TEM and lead to an estimated value of 45 nm. For the LSM95 layer deposited at 810 °C the surface roughness is increased, but the films are still dense. Despite absence of TEM data for the LSM95 layer deposited at ≥810 °C we also expect a slight increase in grain size compared to the 700 °C layer. The following grain widths were therefore used in the quantitative analysis of the tracer profiles: 30, 40 and 45 nm for LSM100 layers and 60, 70 and 75 nm for LSM95 layers, respectively.

3.3 ^{18}O isotope exchange on stoichiometric LSM films

The isotope exchange experiments were conducted at temperatures between 560 °C and 810 °C. The ^{18}O exchange experiments at lower temperatures were performed for 60 min while high temperature anneals in ^{18}O took only 10 min, in order to obtain depth profiles of ^{18}O that still allow determination of the kinetic parameters. Typical ^{18}O isotope fraction depth profiles in a polycrystalline LSM thin film (deposited at 600 °C) are shown in Fig. 4a and b for four different exchange temperatures. Depth profiles consist of two main parts – a steep decrease in the very first nanometers, followed by a shallow isotope concentration decrease. Only at the highest temperature these two regimes can hardly be separated and an almost linear profile is found. If the isotope fraction at the LSM/YSZ interface is still

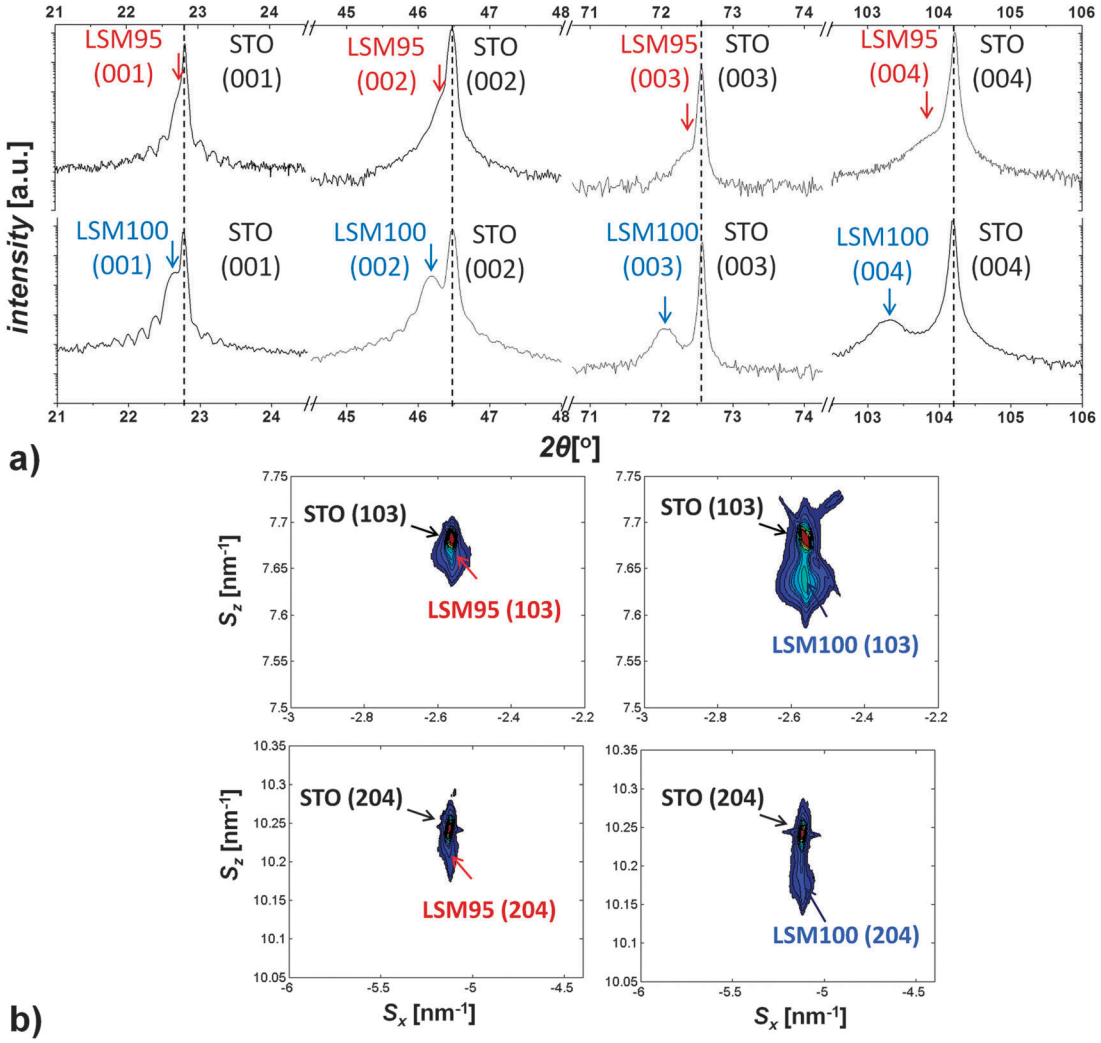

Fig. 2 (a) High resolution XRD 2θ–ω scans of LSM95 and LSM100 layers on STO substrates; (b) reciprocal space maps of LSM95 and LSM100 on STO (001) substrates with the STO reference reflections (–1, 0, 3) and (204).

above the natural abundance (*e.g.* at 810 °C in Fig. 4a) a very shallow profile in YSZ becomes visible, indicating very fast diffusion in YSZ.

The grain size, manipulated by the film deposition temperature, also clearly affects the profiles. As an example, Fig. 4c and d displays the results for LSM100 layers prepared at 600 °C (d = 30 nm) and 860 °C (d = 45 nm) after oxygen exchange at 580 °C. The near-surface parts of the profiles are very similar while a larger grain size causes less ^{18}O concentration in some depth. Profiles measured on epitaxial layers deviate strongly from those of polycrystalline layers. As shown in Fig. 4c, d and 5, the very sharp decrease is not followed by a long diffusion tail. At low temperature, natural abundance is almost reached at the LSM/substrate interface, despite very thin layers (28–29 nm). At high temperatures, however, very high tracer fraction levels penetrate into the films and the profiles become rather flat, despite short diffusion times. Pronounced diffusion in STO is not found.

The absence of the shallow diffusion tail in epitaxial films and the dependence of this part of the diffusion profile on the grain size already indicate an effect of grain boundaries in the overall diffusion kinetics. Profiles strongly resemble those generally found in the type B regime of Harrison's grain boundary diffusion classification.[34,39] Similar isotope exchange depth profiles were also obtained in $SrZrO_3$ pellets, where a fast grain boundary diffusion path was concluded.[40] However, a straightforward analysis of the grain boundary diffusion coefficient according to the model by Whipple–Le Claire[41] (analyzing $\ln f(^{18}O) - x^{6/5}$ slopes) is not possible here: first, we do not have semi-infinite conditions in a single phase but a thin film and fast diffusion in the substrate. Second, we are probably not within the validity range of the model mentioned above, with the total amounts of tracer ions in grain boundaries not being negligible, and diffusion lengths in the grains partly being too large compared to the grain size.

Therefore, a numerical analysis of the measured ^{18}O depth profiles by means of the finite element method (FEM) was performed (COMSOL). The 3D geometry of the model included three domains (Fig. 6), representing diffusion in a grain, along

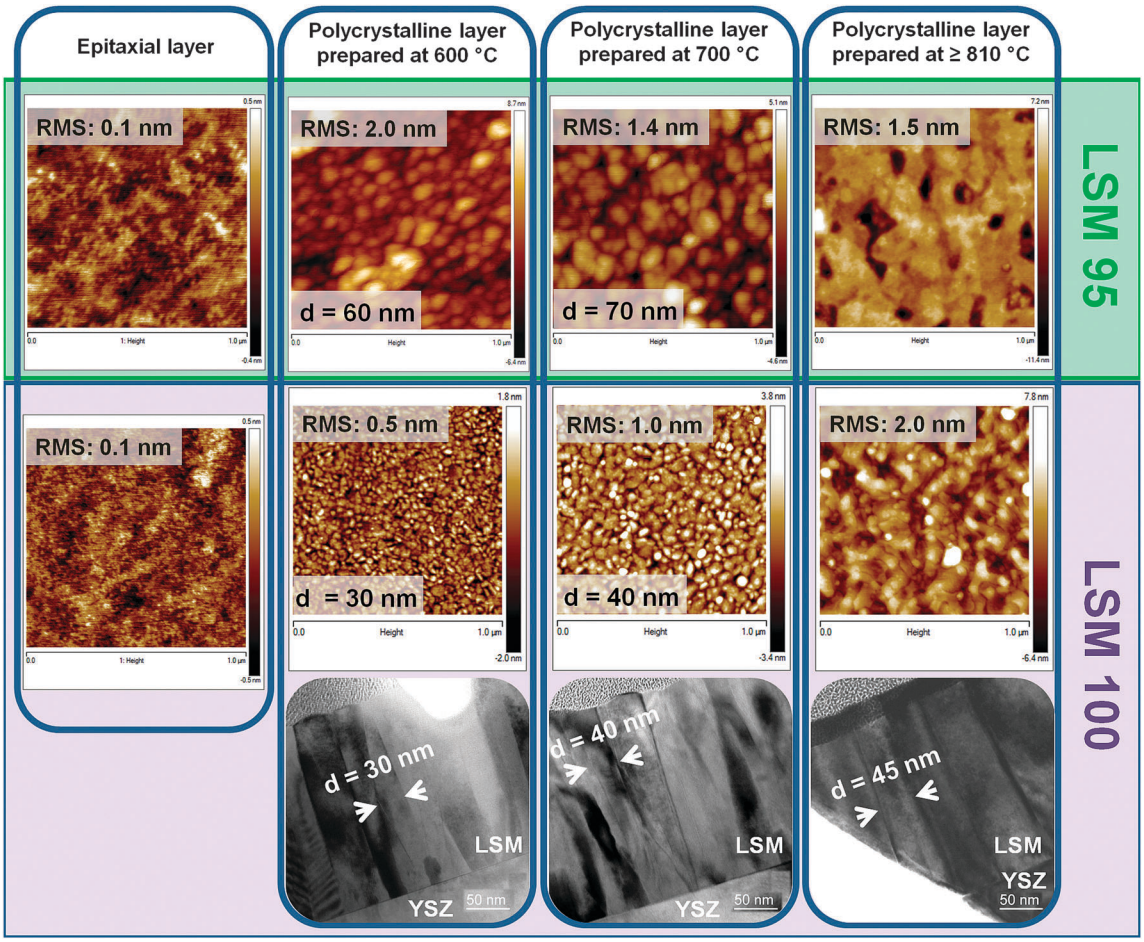

Fig. 3 AFM micrographs (image size: 1 μm × 1 μm) of LSM95 and LSM100 epitaxial and polycrystalline layers prepared at different temperatures demonstrate distinctly different surface microstructure. The bright-field TEM measurements (bottom) on LSM100 polycrystalline layers show the columnar structure and the dependence of the column diameter on the deposition temperature.

the grain boundary and in the YSZ substrate. The width of the grain boundary (δ) was set to 2 nm and the width of a grain (d) was varied in accordance with the approximative values found in the experiments (Section 3.2). For the sake of simplicity, a cylindrically shaped grain was considered, see r.h.s. in Fig. 6. The numerical tool solves Fick's second law of diffusion in all domains, with diffusion coefficients in LSM grains (D_b), LSM grain boundaries (D_{gb}) and YSZ (D_{YSZ}). The boundary conditions of the FEM model reflect that gas exchange is possible at the surface of grains (exchange coefficient k_b) and grain boundaries (k_{gb}). Diffusion thus takes place in the grain, along the boundary, from the grain boundary to the grain and from the LSM layer to the YSZ substrate. Since the profiles were too shallow in YSZ to deduce a diffusion coefficient, D_{YSZ} used in the simulation was calculated from measured conductivity (σ_{ion}) values.

Then FEM calculations with varying D and k values of grain and grain boundary were performed until the best match was found between the calculated isotope profiles and the experimental ones, across the entire set of experimental data. As an additional parameter in the FEM model, the initial value of $f(^{18}O)$ was set to the natural abundance level of 0.00205 for ^{18}O (given by the National Institute of Standards and Technology (NIST)) and the ^{18}O concentration in the gas was assumed to be 97.1% (in accordance with the isotope supplier). The FEM calculations on epitaxial layers were done in a similar manner, though only with a single LSM domain, *i.e.* without grain boundary and without any diffusion in the STO substrate.

First, the concentration depth profile of a polycrystalline film was approximated by a single diffusion process ($D_b = D_{gb}$ and $k_b = k_{gb}$) (green line in Fig. 7a, b). However, in this manner only the steep part of the profile could be described. In a second step, different grain and grain boundary diffusion coefficients were used for the fit ($D_b \neq D_{gb}$ and $k_b = k_{gb}$) (blue line in Fig. 7a, b). Again the measured profile could not be reproduced, since the very high ^{18}O concentration in some depth cannot be explained by fast diffusion in the grain boundaries only. This suggests that also a modified surface exchange coefficient for the grain boundaries has to be involved in the model. Finally, full consideration of all fit parameters with different diffusion and different surface exchange coefficients ($D_b \neq D_{gb}$ and $k_b \neq k_{gb}$) leads to a successful fitting (black lines in Fig. 7). To the best of our knowledge this is the first quantification of the grain boundary surface exchange coefficient of a mixed conducting oxide.

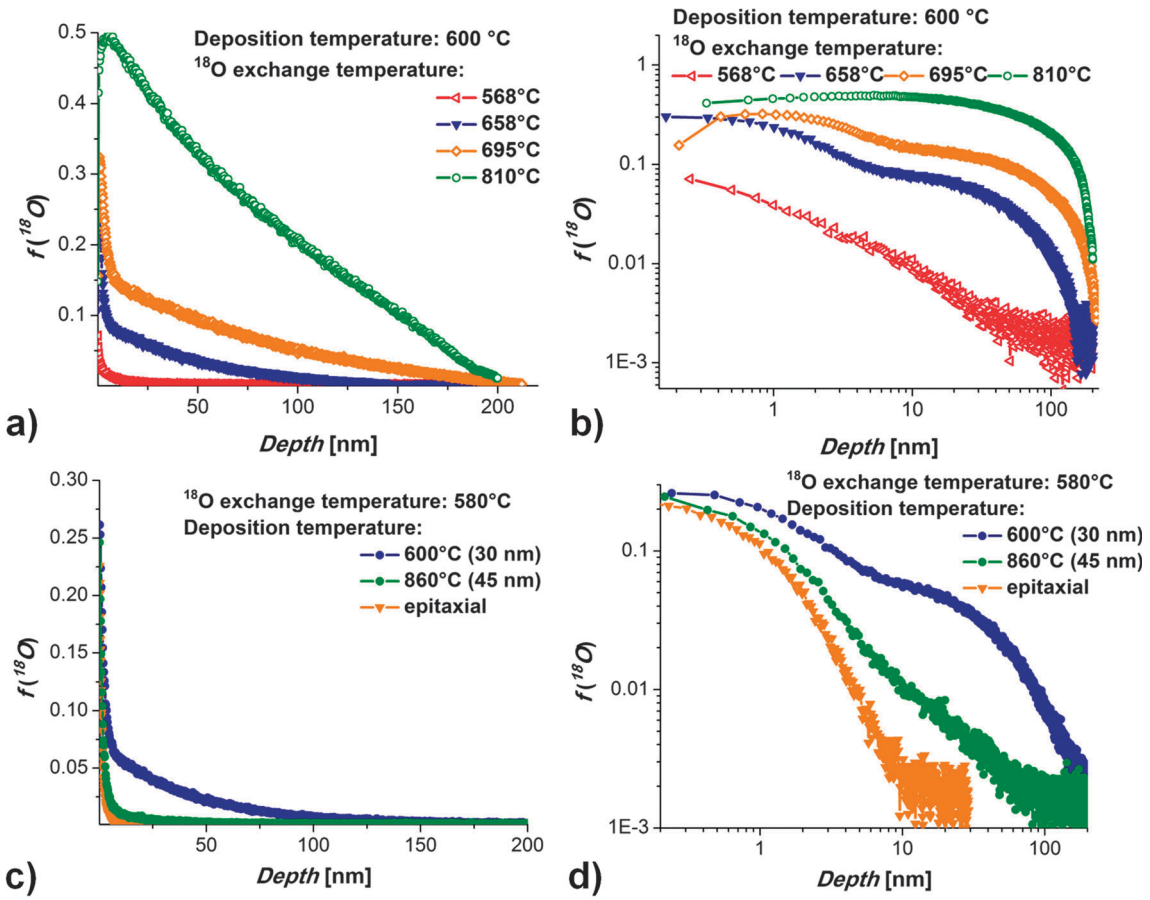

Fig. 4 Typical ^{18}O isotope exchange depth profiles of LSM100 thin films obtained with different isotope exchange temperatures ranging from 568 °C to 810 °C (a and b) and varied layer microstructure (c and d: 30 nm, 45 nm grain size and epitaxial) in linear (a and c) and logarithmic plots (b and d).

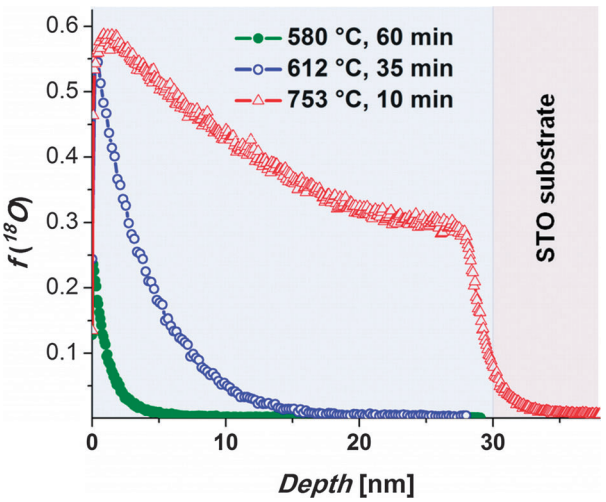

Fig. 5 The ^{18}O isotope exchange depth profiles of epitaxial LSM100 thin films obtained with different isotope exchange parameters.

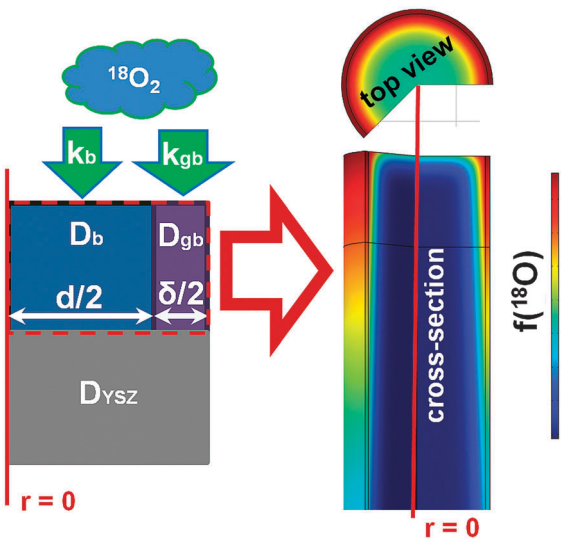

Fig. 6 The sketch of the geometry used in the finite element model to analyze the measured isotope depth profiles.

The same type of FEM analysis of the experimental data was performed for all the polycrystalline samples, each with the corresponding grain size. Fig. 7c and d displays measurement data and fit results for two different grain sizes in linear and logarithmic plots, together with that of the epitaxial layer (see also below). The steep isotope depth profile part corresponding to the grain bulk diffusion is almost the same in all cases while deeper parts strongly depend on the layer microstructure.

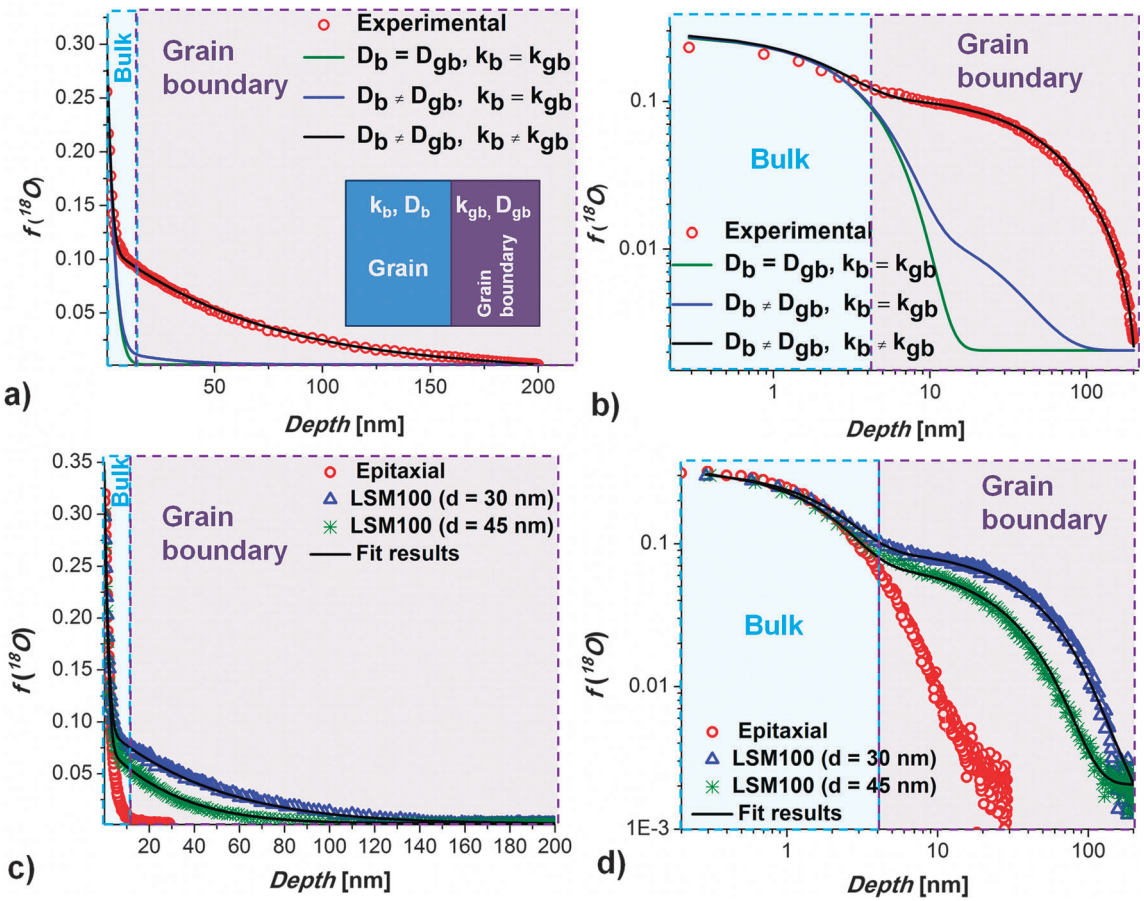

Fig. 7 (a) The measured isotope exchange depth profile (LSM100, d = 30 nm, ^{18}O exchange parameters: T = 695 °C, 10 min) was approximated by the numerical calculation for three cases: only one domain being involved in the model ($D_b = D_{gb}$ and $k_b = k_{gb}$, green line); two domains with different diffusion coefficients used ($D_b \neq D_{gb}$ and $k_b = k_{gb}$, blue line) and two domains with different diffusion and exchange coefficients are employed ($D_b \neq D_{gb}$ and $k_b \neq k_{gb}$) (black line). (b) Isotope exchange depth profile and fitting curves of (a) in a logarithmic plot; (c) tracer exchange depth profiles of LSM100 layers with varied columnar width (30 nm, 45 nm) and the epitaxial layer (^{18}O exchange parameters: 753 °C, 10 min). The black lines are the fitting results obtained from finite element calculations. The first nanometers of the thin films correspond to bulk diffusion and the tail is attributed to grain boundary diffusion. These two contributions are better visible in the logarithmic plot of the isotope exchange depth profile (d).

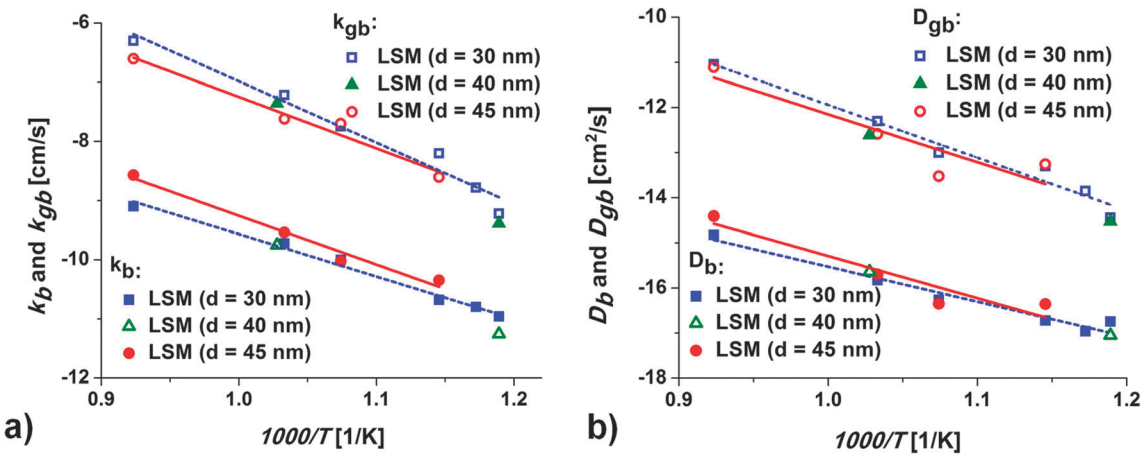

Fig. 8 Arrhenius plots of diffusion (a) and exchange coefficients (b) obtained on LSM100 layers with different microstructure. Much higher oxygen exchange and diffusion coefficients of grain boundaries are found.

The obtained diffusion and surface exchange values for the grain and grain boundaries are plotted in Arrhenius diagrams in Fig. 8. As one can see, both the diffusion coefficients and the surface exchange coefficients of the grain boundaries are orders

Table 1 The averaged activation energies of diffusion E_{D_b} and surface exchange E_{k_b} of grain bulk (b) and grain boundaries (gb) of LSM100 and LSM95 thin films

	E_{D_b} [eV]	$E_{D_{gb}}$ [eV]	E_{k_b} [eV]	$E_{k_{gb}}$ [eV]
LSM100, polycrystalline	1.70	2.22	1.53	1.88
LSM95, polycrystalline	2.04	1.78	1.57	1.70
LSM100, epitaxial	2.55		2.04	
LSM95, epitaxial	2.63		1.97	

of magnitude higher than those of the grain. The enhancement ratios are in the range of 200 to 1000 for D_{gb}/D_b and 200 to 800 for k_{gb}/k_b. Moreover, the diffusion and surface exchange coefficients do not show a significant dependence on the grain size, all data are more or less on the same lines. This suggests that grain boundary widths and grain boundary structure/chemistry of all three layers do not drastically depend on the deposition temperature in the explored range. Moreover, this consistency of the data supports the validity of our proposed model with fast grain boundaries in LSM thin films. The strongly accelerated oxygen exchange and transport kinetics of grain boundaries might become an important contributor to the overall kinetics also in porous LSM electrodes with sub-μm grains, at least in regimes with relevant bulk path, *e.g.* upon significant cathodic polarization.

Still, k and D values slightly spread and the activation energies E_a obtained from Arrhenius plots have to be taken with some care. Fit lines for 30 and 45 nm grains are included in Fig. 8. The activation energies for both grain sizes were averaged and the resulting values for grain bulk (D_b) and grain boundary diffusion (D_{gb}) as well as for both surface exchange coefficients (k_b and k_{gb}) are listed in Table 1. A more detailed discussion of activation energies is given below, together with values found for LSM95 and epitaxial layers.

In the case of epitaxial layers and higher exchange temperatures, only the first part of the depth profile can be fitted with a single diffusion process (Fig. 9a). Obviously, again a second diffusion mechanism is present, even though these additional effects are much less pronounced than for polycrystalline layers. Owing to the supposed absence of grain boundaries in the epitaxial layers, one might attribute the shallow part of the profile to fast diffusion along other extended defects. Extended defects which may contribute to the diffusion of oxygen were also observed in other studies.[22,37] However, in our FEM calculations only the bulk diffusion part was considered, since the density of such supposed additional defects in the LSM epitaxial layers was not known. The D_b and k_b values obtained from the epitaxial layer and averaged values of the polycrystalline LSM100 are plotted in an Arrhenius diagram (Fig. 9b). The similarity of the values supports our model assumption that the near-surface part of the profiles in the polycrystalline layers reflects the bulk diffusion behaviour. Slightly higher D_b and k_b values are found in the epitaxial layers, but statistical relevance of the differences is not proven yet. It might be related to tensile strain, which may change the kinetics,[42] similar to results found for Sr-doped $LaCoO_{3-\delta}$.[33]

3.4 Isotope exchange on A-site deficient LSM films

The ^{18}O exchange experiments were also performed on nominally A-site deficient LSM thin films (LSM95) and typical concentration depth profiles are shown in Fig. 10a (isotope exchange parameters: t = 10 minutes and T = 695 °C). As in the nominally stoichiometric case, the obtained isotope exchange depth profiles depend on the layer microstructure. The grain widths estimated from the AFM and TEM measurements (60, 70 and 75 nm) were used for the FEM simulation of the depth profile, and D and k values for grain and grain boundaries could again be deduced. The results are plotted in Arrhenius type diagrams (Fig. 10b and c). For reasons of comparison averaged data of stoichiometric LSM are also included in Fig. 10b and c. Similar to the stoichiometric case, the diffusion coefficient of grain boundaries is approximately two to three orders of magnitude higher than that of the grain bulk. Also a large difference of k_b and k_{gb} is again found, despite much stronger scattering of k_{gb} data compared to LSM100. Systematic differences between LSM100 and LSM95,

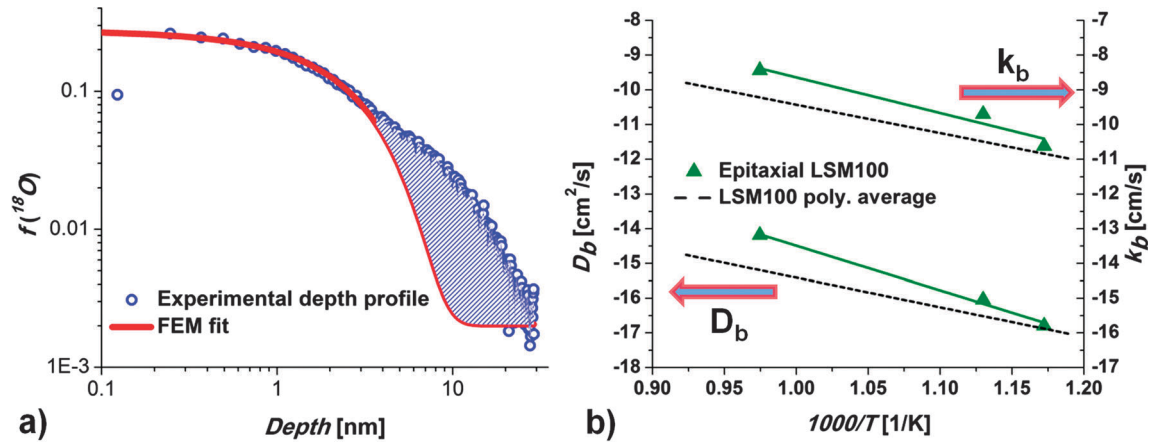

Fig. 9 (a) Isotope depth profile of an epitaxial layer (LSM100, isotope exchange parameters: 695 °C, 10 min) and fit line using D_b and k_b only. The deviating part (blue area) may be caused by extended defects in the epitaxial films; (b) Arrhenius plot of D_b and k_b values obtained from epitaxial (green line) and polycrystalline LSM100 (dashed line) layers.

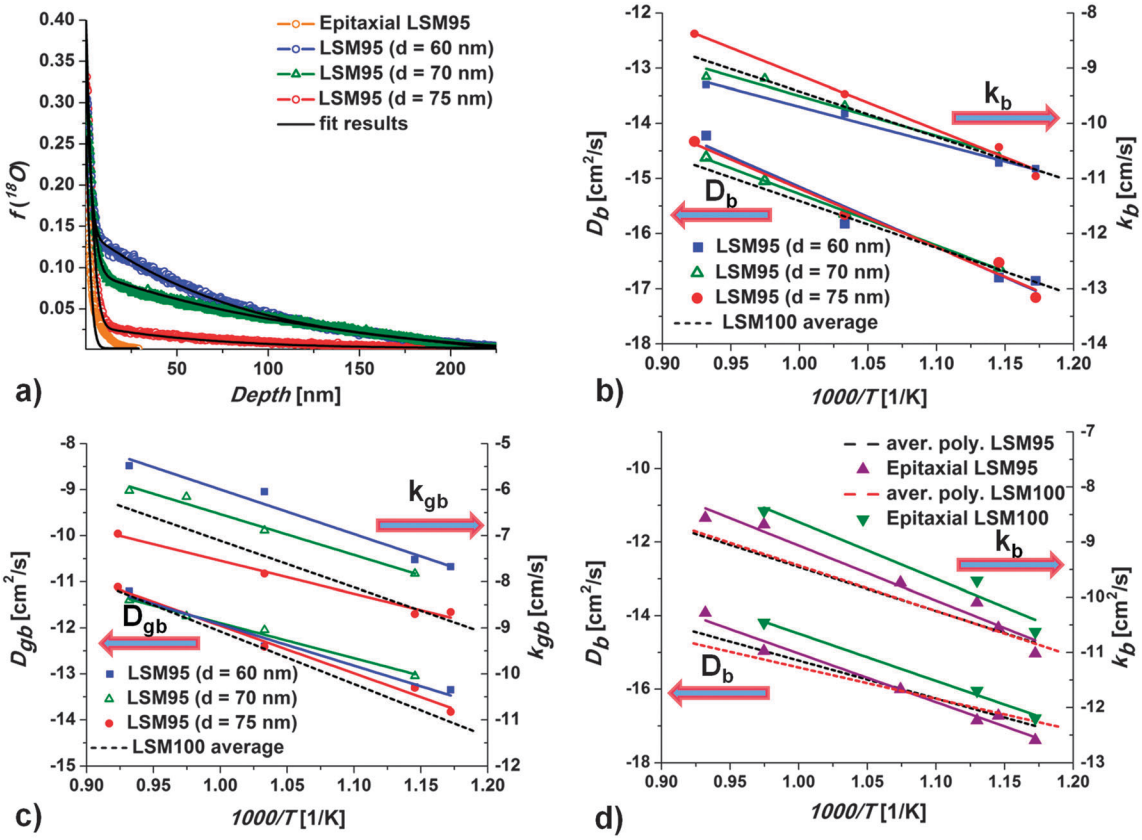

Fig. 10 (a) Isotope exchange depth profiles of A-site deficient LSM layers (LSM95, isotope exchange parameters: 695 °C, 10 min) with varied microstructure. The distinct change of the grain boundary diffusion part in accordance with the microstructure is visible. (b) Arrhenius plot of D_b and k_b of A-site deficient LSM95 thin films; (c) Arrhenius plot of D_{gb} and k_{gb} obtained on LSM95 layers. Average values for LSM100 are given as well; (d) Arrhenius plots of bulk diffusion and surface exchange coefficients obtained on LSM100 and LSM95 epitaxial layers in comparison with polycrystalline LSM (averaged D_b and k_b for polycrystalline layers: LSM100 – red dashed line and LSM95 – black dashed line).

however, are not observed. Again the activation energies of D and k were calculated (lines in Fig. 10b and c) and values averaged for different grain sizes are summarized in Table 1. Profiles of epitaxial LSM95 layers were quantified as described for LSM100 and the resulting D_b and k_b values, together with epitaxial LSM100 and averaged values of polycrystalline LSM100 and LSM95 layers, are included in Fig. 10d. Both, diffusion and exchange coefficients are slightly higher for epitaxial LSM100 but the statistical significance of this difference is not proven yet.

Comparing all activation energies in Table 1 one can conclude that activation energies of k values are smaller than those of D. Differences are of the order of 0.2 to 0.4 eV. A statement on any difference between activation energies of grains and grain boundaries of polycrystalline layers, however, is not possible yet, due to the scatter present in the fitted data. Approximately, we get 2 eV for D values and 1.7 eV for k values. Even the fact that activation energies of epitaxial layers are somewhat higher should not be over-interpreted. All these tracer measurements in thin films and their analysis are far from trivial and include some uncertainties such as very sharp profiles close to the surface at low temperatures, overlap of grain and grain boundary parts, *i.e.* almost linear profiles, at high temperatures (see Fig. 4a), and inaccuracies in determining the grain widths.

In order to check the effect of the grain size and the grain boundary width on the fitting results of an experimentally obtained depth profile of LSM95, the measured data were analyzed with different grain (d = 90, 75 and 60 nm) and grain boundary (δ = 0.5, 1 and 2 nm) widths in the FEM model. The resulting values are listed in Table 2. The variation of the grain width strongly affects the surface exchange coefficients of the grain boundary (k_{gb}), while grain values (D_b, k_b) as well as D_{gb} are much less sensitive. This may explain the strong scatter of the surface exchange values in the LSM95 case, particularly since our model neglects any grain size distribution. The effect of the grain boundary width on k_{gb} and D_{gb} is not surprising and in the range expected when assuming that $\delta \cdot k_{gb}$ and $\delta \cdot D_{gb}$ are the decisive factors for the amount of incorporated tracer ions.

Finally, the activation energies might be compared with those of a previous tracer diffusion study on polycrystalline LSM pellets [34]. There, activation energies for oxygen diffusion in bulk and grain boundaries in the temperature range of 700 °C to 1000 °C were 3.2 eV and 2.8 eV, respectively. In our study, both activation energies are lower. Regarding D_{gb} this might be due to different types of grain boundaries in thin films and polycrystalline pellets, caused by the columnar growth in thin films and the very different temperature treatments (deposition temperature

Table 2 The sensitivity of the results to the variation in grain and grain boundary widths used in the FEM model was analyzed. The experimental results of LSM95 with oxygen exchange at 695 °C (75 nm grain width and 2 nm grain boundary width) were also fitted with different grain widths (from 60 to 90 nm while δ = 2 nm) and grain boundary widths (from 0.5 nm to 2 nm while d = 75 nm) in the FEM model

	D_b [cm^2 s^{-1}]	k_b [cm s^{-1}]	D_{gb} [cm^2 s^{-1}]	k_{gb} [cm s^{-1}]
Grain width d [nm]				
90	2.1×10^{-16}	3.3×10^{-10}	3.9×10^{-13}	1.8×10^{-8}
75	2.2×10^{-16}	3.4×10^{-10}	3.9×10^{-13}	1.5×10^{-8}
60	2.2×10^{-16}	3.6×10^{-10}	3.9×10^{-13}	1.0×10^{-8}
Grain boundary width δ [nm]				
0.5	2.2×10^{-16}	3.4×10^{-10}	8.0×10^{-13}	5.0×10^{-8}
1	2.2×10^{-16}	3.4×10^{-10}	4.0×10^{-13}	2.4×10^{-8}
2	2.2×10^{-16}	3.4×10^{-10}	3.9×10^{-13}	1.5×10^{-8}

much below typical sintering temperatures of pellets). This very different temperature treatment might also cause the severe differences between the absolute k values in ref. 32 and our k_b, ours are two to three orders of magnitude larger. Moreover, in the corresponding analysis of polycrystalline LSM pellets, only fast grain boundary diffusion was included, while fast surface oxygen exchange of grain boundaries was not considered, which further hampers comparison of deduced grain boundary properties. Absolute values of D_b, however, are very close in the temperature regime used in both studies (*e.g.* at *ca.* 800 °C). Hence, one could speculate that at about 700–800 °C a change of the activation energy of D_b takes place and causes the different E_a values found in our study (at lower temperatures) and in ref. 34 (at high temperatures). However, also the very limited temperature range and fit inaccuracies at both ends of our temperature scale might play a role. A comparison of k_{gb} to literature values is not possible since, to the best of our knowledge, this factor has never been measured before.

4. Conclusions

The kinetics of the oxygen exchange reaction and oxide ion diffusion was successfully investigated for nominally stoichiometric and A-site deficient LSM films on YSZ substrates with controlled grain sizes ranging from 30 to 75 nm, as well as for LSM epitaxial films on STO substrates. The diffusion profiles in polycrystalline layers indicate contributions of two parallel paths for surface exchange and diffusion of oxygen – in grain bulk and in grain boundaries. Numerical modelling using the finite element method revealed not only information on grain and grain boundary diffusion, but also on the difference between the kinetics of oxygen exchange on grain surfaces and on grain boundaries. The grain boundary diffusion and surface exchange values obtained from the measurements were approximately two to three orders of magnitude larger than those of the grains. Hence, grain boundaries not only offer fast diffusion paths in LSM but also enable much faster oxygen reduction than the grain surface. Kinetic parameters of epitaxial layers resemble those of grains in polycrystalline layers. All properties hardly depend on the cation stoichiometry employed in this study (LSM95 and LSM100). These data also suggest that grain boundaries might play a significant role in porous LSM electrodes with active bulk path, *e.g.* upon cathodic polarization, and warrant consideration also in designing thin-film based oxide electrochemical energy conversion devices.

Acknowledgements

The authors from Vienna University of Technology gratefully acknowledge Austrian Science Fund (FWF) (projects: F4509-N16, F4502-N16, P21960-N17 and W1243-N16) for the financial support. B. Yildiz and Y. Chen acknowledge the US Department of Energy – Basic Energy Sciences, Grant No. DE-SC000263, for financial support.

References

1 S. M. Haile, *Acta Mater.*, 2003, **51**, 5981–6000.
2 M. Juhl, S. Primdahl, C. Manon and M. Mogensen, *J. Power Sources*, 1996, **61**, 173–181.
3 J. Nielsen and J. Hjelm, *Electrochim. Acta*, 2014, **115**, 31–45.
4 L. C. Baqué, P. S. Jørgensen, K. V. Hansen and M. Søgaard, *ECS Trans.*, 2013, **57**, 2027–2036.
5 Q. Su, D. Yoon, F. Khatkhatay, Q. Jia, A. Manthiram and H. Wang, *Int. J. Hydrogen Energy*, 2013, **38**, 16320–16327.
6 S. P. Jiang, J. P. Zhang, Y. Ramprakash, D. Molosevic and K. J. Wilshier, *J. Mater. Sci.*, 2000, **35**, 2735–2741.
7 S. B. Adler, *Chem. Rev.*, 2004, **104**, 4791–4844.
8 J. Nowotny and M. Rekas, *J. Am. Ceram. Soc.*, 1998, **81**, 67–80.
9 J. Fleig, *Annu. Rev. Mater. Res.*, 2003, **33**, 361–382.
10 V. Brichzin, J. Fleig, H.-U. Habermeier, G. Cristiani and J. Maier, *Solid State Ionics*, 2002, **152–153**, 499–507.
11 T. M. Huber, M. Kubicek, A. K. Opitz and J. Fleig, *J. Electrochem. Soc.*, 2015, **162**, F229–F242.
12 G. J. la O', B. Yildiz, S. McEuen and Y. Shao-Horn, *J. Electrochem. Soc.*, 2007, **154**, B427–B438.
13 R. Radhakrishnan, A. V. Virkar and S. C. Singhal, *J. Electrochem. Soc.*, 2005, **152**, A210–A218.
14 J. Fleig, H.-R. Kim, J. Jamnik and J. Maier, *Fuel Cells*, 2008, **5**, 330–337.
15 T. P. Holme, C. Lee and F. B. Prinz, *Solid State Ionics*, 2008, **179**, 1540–1544.
16 P. Plonczak, D. Risskov Sorensen, M. Sogaard, V. Esposito and P. Vang Hendriksen, *Solid State Ionics*, 2012, **217**, 54–61.
17 W. Lee, J. Woo Han, Y. Chen, Z. Cai and B. Yildiz, *J. Am. Chem. Soc.*, 2013, **135**(21), 909–7925.
18 H. Y. Lee, W. S. Cho, S. M. Oh, H.-D. Wiemhöfer and W. Göpel, *J. Electrochem. Soc.*, 1995, **142**, 2659–2664.
19 M. J. Jorgensen, P. Holtappels and C. C. Appels, *J. Appl. Electrochem.*, 2000, **30**, 411–418.
20 A.-K. Huber, M. Falk, M. Rohnke, B. Luerssen, M. Amati, L. Gregoratti, D. Hesse and J. Janek, *J. Catal.*, 2012, **294**, 79–88.
21 L. Yan, K. R. Balasubramaniam, S. Wang, H. Du and P. A. Salvador, *Solid State Ionics*, 2011, **194**, 9–16.

22 L. Yan and P. A. Salvador, *ACS Appl. Mater. Interfaces*, 2012, **4**, 2541–2550.
23 K. Katsiev, B. Yildiz, B. Kavaipatti and P. A. Salvador, *ECS Trans.*, 2009, **25**, 2309–2318.
24 K. Katsiev, B. Yildiz, K. Balasubramaniam and P. A. Salvador, *Appl. Phys. Lett.*, 2009, **95**, 092106.
25 K. Opitz, A. Schintlmeister, H. Hutter and J. Fleig, *Phys. Chem. Chem. Phys.*, 2010, **12**, 12734–12745.
26 J. Fleig, A. Schintlmeister, A. K. Opitz and H. Hutter, *Scr. Mater.*, 2011, **65**, 78–83.
27 K. Opitz, A. Lutz, M. Kubicek, F. Kubel, H. Hutter and J. Fleig, *Electrochim. Acta*, 2011, **56**, 9727–9740.
28 K. Opitz, M. Kubicek, S. Huber, T. Huber, G. Holzlechner, H. Hutter and J. Fleig, *J. Mater. Res.*, 2013, **28**, 2085–2105.
29 H. Kishimoto, N. Sakai, K. Yamaji, T. Horita, M. E. Brito, H. Yokokawa, K. Amezawa and Y. Uchimoto, *Solid State Ionics*, 2008, **179**, 1343–1346.
30 T. Horita, K. Yamaji, N. Sakai, H. Yokokawa, T. Kawada and T. Kato, *Solid State Ionics*, 2000, **127**, 55–65.
31 I. Yasuda, K. Ogasawara, M. Hishinuma, T. Kawada and M. Dokiya, *Solid State Ionics*, 1996, **86–88**, 1197–1201.
32 R. A. De Souza, J. A. Kilner and J. F. Walker, *Mater. Lett.*, 2000, **43**, 43–52.
33 M. Kubicek, Z. Cai, W. Ma, B. Yildiz, H. Hutter and J. Fleig, *ACS Nano*, 2013, **7**, 3276–3286.
34 S. Fearn, J. C. H. Rossiny, J. A. Kilner and J. R. G. Evans, *Solid State Ionics*, 2012, **211**, 51–57.
35 G. Holzlechner, M. Kubicek, H. Hutter and J. Fleig, *J. Anal. At. Spectrom.*, 2013, **28**, 1080–1089.
36 M. Kubicek, G. Holzlechner, A. K. Opitz, S. Larisegger, H. Hutter and J. Fleig, *Appl. Surf. Sci.*, 2014, **289**, 407–416.
37 O. I. Lebedev, G. Van Tendeloo and S. Amelinckx, *Int. J. Inorg. Mater.*, 2001, **3**, 1331–1337.
38 Y. Takamura, R. V. Chopdekar, E. Arenholz and Y. Suzuki, *Appl. Phys. Lett.*, 2008, **92**, 162504.
39 L. G. Harrison, *Trans. Faraday Soc.*, 1961, **57**, 1191–1199.
40 C. Nivot, C. Legros, B. Lesage, M. Kilo and C. Argirusis, *Solid State Ionics*, 2009, **180**, 1040–1044.
41 A. D. Le Claire, *Br. J. Appl. Phys.*, 1963, **14**, 351–356.
42 H. Jalili, J. W. Han, Y. Kuru, Z. Cai and B. Yildiz, *J. Phys. Chem. Lett.*, 2011, **2**, 801–807.